

NON EQUILIBRIUM THERMODYNAMICS AND COSMOLOGICAL PANCAKES FORMATION

ROMAIN TEYSSIER, JEAN-PIERRE CHIÈZE

Centre d’Etudes de Saclay, DAPNIA, Service d’Astrophysique, 91191, Gif sur Yvette,
France.

JEAN-MICHEL ALIMÌ

Laboratoire d’Astrophysique Extragalactique et de Cosmologie, CNRS URA 173,
Observatoire de Paris-Meudon, 92195-Meudon, France.

ABSTRACT

We investigate the influence of non equilibrium thermodynamics on cosmological structure formation. In this paper, we consider the collapse of planar perturbations usually called “Zel’dovich pancakes”. We have developed for that purpose a new two fluids (gas and dark matter) hydrodynamical code, with three different thermodynamical species: electrons, ions and neutral particles ($T_e \neq T_i \neq T_n$). We describe in details the complex structure of accretion shock waves. We include several relevant processes for a low density, high temperature, collisional plasma such as non-equilibrium chemical reactions, cooling, shock heating, thermal energy equipartition between electrons, ions and neutral particles and electronic conduction. We find two different regions in the pancake structure: a thermal precursor ahead of the compression front and an equipartition wave after the compression front where electrons and ions temperatures differ significantly. This complex structure may have two interesting consequences: pre-heating of unshocked regions in the vicinity of massive X-ray clusters and ions and electrons temperatures differences in the outer regions of X-rays clusters.

Subject headings: Cosmology: theory – hydrodynamics – methods: numerical

1. INTRODUCTION.

The thermodynamical state of the Intergalactic Medium is of primary importance to study the formation and the evolution of cosmic structures. In the dense central regions of galaxy clusters, cooling is likely to play a dominant role. In the outer regions, the density is rather low and allows an adiabatic treatment of gas dynamics. In the same time, non-equilibrium thermodynamics occurs in this in this hot and diffuse plasma. Indeed, for high temperatures ($T \simeq 10^8 K$) and low densities ($n_e \simeq 10^{-4} cm^{-3}$), typical values found in the outer regions of large X-rays clusters (Markevitch et al. 1996), the time-scale for electrons and ions to reach thermodynamical equilibrium through Coulomb collisions is about $t_{ei} \simeq 4 \times 10^9 yr$, comparable to the Hubble time.

In order to study these low density regions where strong departure from thermodynamical equilibrium is expected, it has been pointed out by Kang et al. (1994) that an Eulerian code is well suited. In this paper, we therefore present a new Eulerian code and then use it to model non equilibrium processes during the formation of Zel'dovich pancakes.

Pancakes appeared for a long time as fundamental tools in Cosmology. Zel'dovich (1970) was the first to point out that sheet-like structures could form through gravitational instability. These pancakes was first motivated by the neutrino-dominated scenario of structures formation, where they form naturally. Although this scenario seems today in difficulties with observations, walls and filaments are still observed in both observational and theoretical studies based on other more popular scenarios like Cold Dark Matter or Mixed Dark Matter (Cen & Ostriker 1992, Peebles 1993). Therefore, pancake geometry is not only an idealized case for testing numerical codes, but is also cosmologically relevant.

Hydrodynamics of pancake collapse have been studied by several authors (Bond *et al.* 1984, Shapiro & Struck-Marcell 1985, Anninos & Norman 1994) with the baryon component, obeying the hydrodynamics equations and coupled to collisionless dark matter particles. Different numerical schemes for modeling the hydrodynamical equations were used. Bond *et al.* (1984) and Anninos and Norman (1994) used an Eulerian scheme, while Shapiro and Struck-Marcell (1985) used a Lagrangian scheme. All these studies were dedicated to the calculation of the cooled mass fraction formed via pancake collapse. On the contrary to the previous studies, we focus in this paper on non-equilibrium phenomena which are enhanced in the large scale, low density part of pancakes. We introduce three temperatures to describe the thermodynamic evolution of electrons, ions and neutral particles. Chemical evolution of the primordial Hydrogen-Helium gas is solved without assuming ionization-recombination equilibrium. Moreover, we also model electronic conduction with a flux-limited diffusion scheme.

This paper is organized as follows. In section 2 we present the basics equations governing the system and we describe our hydrodynamical code with validating tests. In section 3 we present the results of simulations concerning the formation of pancakes. We show that, in the general case, a complex structure forms, with a thermal wave escaping out of the shocked region together with an equipartition wave where electrons and ions temperatures can differ significantly. We finally discuss in section 4 the rôle of various parameters, such as the baryons density parameter Ω_B , the wavelength of the initial perturbation L and the pancake collapse epoch a_c .

2. PHYSICS AND NUMERICAL METHODS

2.1. Basic equations

The equations are written in comoving coordinates, through the transformation $\mathbf{r} = a(t)\mathbf{x}$ where $a(t)$ is the expansion factor. We take here a as the time variable. We assume an Einstein-de Sitter universe, with zero cosmological constant. The velocity of Dark Matter particles and fluid elements are respectively $\mathbf{v} = \frac{D\mathbf{x}}{Da}$ and $\mathbf{u} = \frac{D\mathbf{x}}{Da}$. Dark matter particles satisfy the equations of motion

$$\frac{D\mathbf{v}}{Da} = -\frac{2 - \Omega/2}{a}\mathbf{v} - \frac{3\Omega}{2a^2}\nabla_x\phi \quad (1)$$

Ω is the background density parameter, and H the Hubble constant (both parameters are time-dependent quantities). For Lagrangian fluid elements, one has to add the pressure term

$$\frac{D\mathbf{u}}{Da} = -\frac{2 - \Omega/2}{a}\mathbf{u} - \frac{3\Omega}{2a^2}\nabla_x\phi - \frac{1}{a^4H^2}\frac{\nabla_x P}{\rho_B} \quad (2)$$

and to consider the continuity equation

$$\frac{1}{\rho}\frac{D\rho}{Da} = -\left(\frac{3}{a} + \nabla_x \cdot \mathbf{u}\right) \quad (3)$$

The total pressure $P = P_e + P_i + P_n$ is the sum of the electrons, ions and neutral particles partial pressures. The gravitational potential satisfies the Poisson equation

$$\nabla_x^2\phi = \frac{\rho - \bar{\rho}}{\bar{\rho}} = \delta \quad (4)$$

where $\rho = \rho_D + \rho_B$ is the total mass density and $\bar{\rho}$ is the mean background total mass density. Throughout this paper, densities refer to proper physical quantities and not to comoving quantities. We consider six chemical species of number densities of each species n_e , n_{HI} , n_{HII} , n_{HeI} , n_{HeII} and n_{HeIII} . The partial pressures are then related to the kinetic temperatures as $P_e = n_e k T_e$, $P_i = (n_{HII} + n_{HeII} + n_{HeIII}) k T_i$ and $P_n = (n_{HI} + n_{HeI}) k T_n$.

We define the specific volume $V = 1/\rho_B$, occupied by a unit mass of baryons. The specific internal energy E_α for each thermodynamical specy ($\alpha = e, i, n$) follows then the equation of state for a mono-atomic gas ($\gamma = 5/3$)

$$E_\alpha = \frac{1}{\gamma - 1} P_\alpha V \quad (5)$$

and satisfies the first law of thermodynamics

$$\frac{DE_\alpha}{Da} = -(\gamma - 1)E_\alpha \left(\frac{3}{a} + \nabla_x \cdot \mathbf{u} \right) + \frac{DQ_\alpha}{Da} \quad (6)$$

The first term in the right hand-side of equation (6) is the PdV work due to expansion and comoving compression and the last term is the net heat source per unit mass due to different irreversible, non adiabatic processes.

2.2. Thermodynamical processes

The thermodynamical evolution of the plasma is treated in a self-consistent way with its chemical evolution, without assuming ionization - recombination equilibrium. The thermodynamical processes modeled in our code are: shock heating for ions and neutral particles, cooling and thermal conduction for electrons and equipartition between electrons, ions and neutral particles.

We have used the collisional ionization rate and the radiative recombination rate given by Cen (1992) which include correction terms for very high temperatures. As we have to deal with three different kinetic temperatures for the gas, the actual rates are obtained by using the *reduced temperature* of the two reactants (Draine 1980; Draine & Katz 1986). In the case of proton-electron interaction, this writes $T_{ei} = \left(\frac{m_p T_e + m_e T_i}{m_p + m_e} \right)$. In practice, if $T_e \simeq T_i$, this implies a small correction of the order of m_e/m_p . But in some extreme cases where $T_i \gg T_e$, this correction is not negligible. We also considered classical cooling processes such as ionization, recombination and line cooling, together with bremsstrahlung and Compton cooling by the Cosmic Background Radiation. The cooling rates are again those of Cen

(1992), modified using the reduced temperature. Note that cooling results in an internal energy loss for the electrons only.

Massive particles (ions and neutral) share most of the entropy deposition due to shock heating. The electrons are mainly heated by energy exchange with the latter species. As a matter of fact, in a perfect fluid, shocks are discontinuities in the flow, obeying Rankine-Hugoniot relations. They imply that the post-shock temperature for a given particle species “i” is $T \propto m_i \mathcal{D}^2$, where \mathcal{D} is the up-wind fluid velocity in the rest-frame of the shock front. Consequently, the post-shock electron temperature is m_e/m_p , much lower than the ions post-shock temperature and negligible compared to the final equilibrium temperature. We therefore neglect electrons shock heating. Shock heating will be treated in the code using the artificial viscosity method (Richtmyer & Von Neuman 1974), which includes a linear and a quadratic viscous term. This can be written in one dimension, *and in one dimension only*, as a viscous pressure, that we add to the usual ions (resp. neutral particles) thermal pressure.

$$P_{i,visc} = P_i \left(C_1 \epsilon + C_2 \epsilon^2 \right) \quad \text{where} \quad \epsilon = -\frac{a \Delta x}{c_{s,i}} \left(3 + a \nabla_x \cdot \mathbf{u} \right) \quad (7)$$

The equivalent energy source term entering equation (6) for ions is given by

$$\frac{DQ_{i,visc}}{Da} = -P_{i,visc} V \left(\frac{3}{a} + \nabla_x \cdot \mathbf{u} \right) \quad (8)$$

Similar equations apply for neutral particles. C_1 and C_2 are two constants determined a posteriori by numerical tests, and Δx is the mesh spacing.

Electrons are heated by ions through Coulomb interactions, and by neutral particles through short-range forces. The equipartition rates are computed using the momentum transfer cross section of the different interacting species. For example, the net kinetic energy transfer rate per unit mass between electrons and protons is (Spitzer 1962)

$$\frac{DQ_{p \rightarrow e}}{Da} = -\frac{DQ_{e \rightarrow p}}{Da} = -k (T_i - T_e) \left(\frac{4(2\pi)^{1/2} e^4 m_e^{1/2} \ln \Lambda_{ep}}{m_p (kT_{ei})^{3/2}} \right) \frac{n_e n_p}{\rho_B a H} \quad (9)$$

where T_{ei} and $\ln \Lambda_{ep}$ are respectively the reduced temperature and the Coulomb logarithm of the two interacting particles. The heat transfer rates between the other chemical species can be expressed in a similar form (Draine 1980; Chièze, Pineau des Forêts & Flower 1998).

When electronic temperature gradients are present in the flow, a net heat flux appears,

written here in its “classical” form

$$\mathbf{q}_{cl} = -\frac{1}{a}\kappa_e \nabla_x T_e \quad (10)$$

with conductivity coefficient (Spitzer 1962)

$$\kappa_e = 1.84 \times 10^{-5} \frac{T_e^{5/2}}{\ln \Lambda} \quad (11)$$

In the case of very high fluxes (very steep gradients *or* very high temperatures and low densities), the flux saturates to a value corresponding to a free transport of the electron internal energy at a fraction of the electrons sound speed. We choose the flux-limited diffusion scheme described in Cowie and McKee (1977). The formulae we use here are the followings

$$\mathbf{q}_e = \frac{\mathbf{q}_{cl}}{1 + q_{cl}/q_{sat}} \quad (12)$$

where the maximum (saturated) value of the heat flux is given by

$$q_{sat} = 0.4 \left(\frac{2kT_e}{\pi m_e} \right)^{1/2} n_e k T_e \quad (13)$$

The heat source (or sink) which enter equation (6), due to electronic conduction, is finally given by

$$\frac{DQ_e}{Da} = -\frac{1}{a^2 H} \nabla_x \cdot \mathbf{q}_e \quad (14)$$

Ions are also able to transfer heat through ions conductivity, but the conduction coefficient is reduced by the factor $(m_e/m_p)^{1/2}$, so this extra heat flux is much less effective. Moreover the average kinetic velocity for the ion gas after the shock front is lower than the shock velocity. Consequently ions do not cross the shock front, except for a few supra-thermal particles. The thermal flux due to ions is therefore neglected. In the opposite, the electrons sound speed is $(m_p/m_e)^{1/2}$ times larger than the shock wave velocity (Zel’dovich & Raizer 1966). The electron heat flux therefore crosses easily the compression front and pre-heats efficiently the cold gas ahead of the shock. Finally, ions will in turn be heated through Coulomb energy exchange with electrons.

The capacity of electron to transport heat via conduction is dramatically limited in presence of magnetic fields. Since no evidence for strong magnetic fields has come to our knowledge, we expect electronic conduction to occur at this rate. But during the collapse, and more specifically during shock wave formation, a strong enough magnetic field could be generated and reduce the effect of conduction. Therefore, we made simulations with and without electronic conduction.

2.3. Numerical technics

We present here our 1D hydrodynamical Eulerian code. The extension of this code to a fully 3D hydrodynamical scheme is presented in a companion paper (Chièze, Alimi & Teyssier (1998)).

Our code is based on the operator splitting method with four consecutive steps. The first step is called the **Gravity step**. It solves the Vlasov-Poisson equations for Dark Matter particles and calculates the gravitational potential. The second step is called the **Lagrangian step**, and solves the adiabatic Hydrodynamics equations in their Lagrangian form. The third step is called **Eulerian step**, it calculates the projected hydrodynamics quantities on the fixed Eulerian grid from the perturbed Lagrangian grid. The last step is called the **Dissipative step**; it computes all local dissipative processes, cell by cell, using the densities resulting from the two previous steps. Our code in its final version is of second order accuracy both in time and in space. It allows great stability and efficiency. We present here its general features. We then show tests which demonstrate its ability to handle cosmological simulations.

2.4. General Presentation of the Code

We consider a two-fluid system (Dark-Matter and Baryons). The physical variables associated to Dark Matter particles (superscript j) are x^j , the position of particle j , v^j , the velocity of particle j . The discrete values of the flow on the grid (superscript i) are M^i , the total baryons mass in cell i , N_X^i , the total numbers of particle X in cell i , S_e^i , S_i^i , S_n^i , respectively the total entropy of electrons, ions and neutral particles in cell i , u_x^i , the velocity in the x-direction of interface i and finally r_x^i , the position in the x-direction of interface i .

Mass, particles numbers and entropies are zone-centered, while the velocity is face-centered. This is the well-known staggered mesh method (Stone & Norman 1992). It

allows better accuracy when computing finite differences, and also reduces the number of interpolation to calculate fluxes, which are defined at cell interfaces. The variable r_x^i is usual in pure Lagrangian schemes, it allows to compute densities, while the mass remains constant. As we will see below, it also improves the accuracy of both time integration and flux interpolation.

The specific entropy S_α is defined for each thermodynamical specy α as $S_\alpha = E_\alpha V^{\gamma-1}$. Using the energy equation (6), the time-derivative of S_α reduces then to

$$\frac{DS_\alpha}{Da} = \frac{S_\alpha}{E_\alpha} \frac{DQ_\alpha}{Da} \quad (15)$$

The thermodynamical evolution of baryons is computed using the entropy equation (15) rather than the energy equation (6). This method does not introduce any numerical spurious dissipation effects due to expansion or compression. Consequently, an adiabatic flow ($DQ_\alpha/Da = 0$) is strictly adiabatic during the Lagrangian step.

2.5. Gravity Step

We evolve the Dark Matter particles using a Particle-Mesh algorithm (Hockney & Eastwood 1981) with a Predictor-Corrector scheme. This time-integrator ensures both second-order time-accuracy and variable time-stepping. Let us suppose that particles positions and velocities are known at a given time a . We compute the predicted positions at time $a + \Delta a$ with $(x^j)^{(1)} = x^j + \Delta a v^j$. The superscript (1) means that the quantity is the predicted quantity evaluated at time $a + \Delta a$. The Dark Matter density fields ρ^i and $(\rho^i)^{(1)}$ are then evaluated with a CIC interpolation scheme. In order to solve now the Poisson equation, we need to know also the predicted Baryon density field $(\rho_B^i)^{(1)}$. This one is deduced from the Baryon density and velocity fields at time a by solving the continuity equation. From the gravitational potential ϕ at time a and from its predicted quantity $(\phi)^{(1)}$, at time $a + \Delta a$, we deduce then the forces F^j and $(F^j)^{(1)}$ for the Dark Matter particles by inverse interpolation, at respectively positions x^j and positions $(x^j)^{(1)}$. Velocities and positions for Dark Matter particles are finally updated according to the formula

$$\frac{(v^j)^{(2)} - v^j}{\Delta a} = -\frac{2 - \Omega/2}{a} \frac{(v^j)^{(2)} + v^j}{2} - \frac{3\Omega}{2a^2} \frac{F^j + (F^j)^{(1)}}{2} \quad (16)$$

$$\frac{(x^j)^{(2)} - x^j}{\Delta a} = \frac{(v^j)^{(2)} + v^j}{2} \quad (17)$$

where a is now the *centered* expansion factor $a + \Delta a/2$, Ω is the corresponding density parameter and $(x^j)^{(2)}$ and $(v^j)^{(2)}$ are the updated position and velocity for particle j at time $a + \Delta a$.

2.6. Lagrangian Step

At this step we solve the adiabatic Hydrodynamics equations, together with shock heating and electronic conduction. All the quantities involved in these equations depend on spatial derivatives of the flow. These ones are estimated with a finite-difference scheme. Chemical, cooling and equipartition processes which are purely local (i.e. they don't depend on spatial derivatives of the flow) are solved in the Dissipative step.

The adiabatic Hydrodynamics equations for interface i write for an explicit scheme (first order: superscript (1)) as

$$\left(\frac{\Delta r_x^i}{\Delta a} \right)^{(1)} = u_x^i \quad (18)$$

$$\left(\frac{\Delta u_x^i}{\Delta a} \right)^{(1)} = -\frac{2 - \Omega/2}{a} u_x^i - \frac{3\Omega}{2a^2} \frac{\phi^i - \phi^{i-1}}{\Delta x} - \frac{2\Delta x^2}{aH^2} \frac{P^i - P^{i-1}}{M^i + M^{i-1}} \quad (19)$$

where the pressure P^i includes electron, ions and neutral partial pressures, and the artificial viscous pressures for shock heating (equation 7). The entropy equations due to electronic conduction for electrons, and to shocks heating for ions and neutral particles for the cell i are derived in a similar way by finite differencing equations (8), (12) and (15). Only the variables $(r_x^i, u_x^i, S_e^i, S_i^i, S_n^i, i = 1, N)$ are coupled, the total mass and total numbers of particles remains strictly constant during the Lagrangian step. In order to integrate the previous equations, we have to compute the increments (designed by Δ) of each variables between time a and time $a + \Delta a$. Several methods are possible. The most straightforward one is to use directly the explicit estimation we already mentioned (first order method; see Stone & Norman 1992). It however needs a rather strong condition on the time step in order to be stable, namely the Courant condition. The implicit method, on the other hand, allows much larger time-steps. It is very stable, but very CPU-time consuming, because it implies to invert a band matrix. In this paper, we have preferred to use a second-order

time integrator scheme inspired by the implicit method. It consists to derive second order increments by Taylor expanding the first order increments given by equations (18) and (19), with respect to the flow variables, namely r_x , u_x , S_e , S_i and S_n . For example, the acceleration terms for interface i , which depends on u_x^{i-1} , r_x^{i-1} , S_e^{i-1} , S_i^{i-1} , S_n^{i-1} , u_x^i , r_x^i , S_e^i , S_i^i , S_n^i , u_x^{i+1} , and r_x^{i+1} yields the following second order (superscript (2)) estimation of the velocity increment

$$\begin{aligned} \left(\frac{\Delta u_x}{\Delta a}\right)^{(2)} &= \left(\frac{\Delta u_x}{\Delta a}\right)^{(1)} + \frac{\Delta a}{2} \left[\left(\frac{\Delta r_x}{\Delta a}\right)^{(1)} \frac{\partial}{\partial r_x^{i-1}} \left(\frac{\Delta u_x}{\Delta a}\right)^{(1)} \right] \\ &+ \frac{\Delta a}{2} \left[\left(\frac{\Delta u_x}{\Delta a}\right)^{(1)} \frac{\partial}{\partial u_x^{i-1}} \left(\frac{\Delta u_x}{\Delta a}\right)^{(1)} \right] \\ &+ \dots \end{aligned} \quad (20)$$

where only the partial derivative with respect to the r_x^{i-1} and u_x^{i-1} terms has been written for sake of simplicity. It is important to add partial derivatives of the first order increment with respect to all variables involved in equation (19). This method differs from the standard “predictor-corrector” scheme, since the second order correction presented here is computed analytically using partial derivatives of the first order increments. At the end of the Lagrangian step, we have the new entropies, the new velocities and the new interface positions. Mass and numbers of particles have not been modified.

Finally the time-step is controlled using usual methods (see e.g. Stone & Norman 1992), with a constraint for each of the following processes: artificial viscosity, conduction, gravity and gas dynamics. For example, for a pure gas dynamics problem, the time-step is controlled by the following criterion

$$\Delta a = C_0 \min \left(\frac{a^2 H \Delta x}{\sqrt{(a^2 H u)^2 + c_s^2 + c_{visc}^2}} \right) \quad (21)$$

where c_s is the adiabatic sound speed, and c_{visc} is related to the viscous pressure by the formula

$$c_{visc} = 4 \sqrt{\frac{\gamma P_{visc}}{\rho_B}} \quad (22)$$

The factor 4 in the last equation corresponds to the stability criterion for a viscous fluid with constant viscosity coefficient ν ; the equations of motion in this case are analogous to

the well documented diffusion equation, for which the stability criterion is established as $\Delta t \leq (\Delta x)^2/(4\nu)$ (see Stone & Norman 1992). The Courant safety coefficient C_0 has to be chosen less than 0.5 in order for an explicit scheme (first order) to be stable, and even smaller (typically 0.1) to be accurate. On the contrary, our second order scheme remains stable and accurate, even with the ultimately large time-stepping given by $C_0 = 1$ (see the tests section).

2.7. Eulerian Step

We now want to re-map all variables from the disturbed Lagrangian grid to the fixed Eulerian one. This step has to conserve mass, numbers of particles, internal energies of electrons, ions and neutral particles, and momentum. We defined the left-centered momentum in cell i as $P_L^i = M^i u_x^i$ and the right-centered momentum in cell i as $P_R^i = M^i u_x^{i+1}$, in order to deal only with zone-centered quantities. The projection step consists then to solve the advection equation (written here only for the mass)

$$\frac{\partial}{\partial t} \int \rho dV = - \int \rho \mathbf{u} \cdot d\mathbf{S} \quad (23)$$

for each zone which has a control volume $V^i = (\Delta x)^2 (r_x^{i+1} - r_x^i)$. A finite difference approximation of this integral equation is

$$M_P^i - M^i = \Delta M_x^i - \Delta M_x^{i+1} \quad (24)$$

where M_P^i are the projected masses on the Eulerian grid and ΔM_x^i is the advected mass through interface i . This scheme is strictly conservative for the projected variables by construction. The main problem of the advection procedure arises when one calculates the total mass contained in the advected volumes. To do so, we have to calculate a realistic mass distribution within each cell, and then integrate this distribution in the advected volume. There are basically three tractable methods: uniform, linear and parabolic distributions. These three methods are known as the Donor Cell method, the Van Leer method (Van Leer 1977) and the Piecewise Parabolic Interpolation (PPI) method (Woodward & Colella 1985). The first one is very simple but quite diffusive. It is first order accurate in space. The two other methods are much less diffusive and are respectively second and third order accurate in space. The PPI method is the most time consuming, while Van Leer method offers a good compromise between accuracy and efficiency (see Stone & Norman (1992) for a general description).

We calculate interpolation functions for mass, momentum and total internal energy ($E = E_e + E_i + E_n$) only. The numbers of particles within the cell are distributed according to the mass distribution, and internal energies for the 3 species are distributed according to the total internal energy distribution. This ensures exact mass and charge conservation within each cell, and avoids spurious decoupling between the 3 temperatures. The entropy are then updated from the projected internal energy, and the velocity is updated from the left-centered projected momentum, the right-centered projected momentum and the projected mass according to the formula

$$u_x^i = \frac{P_R^{i-1} + P_L^i}{M^{i-1} + M^i} \quad (25)$$

This equation yields an exact momentum conservation. All new Hydrodynamics variables on the Eulerian grid are now known.

2.8. Dissipative Step

We solve now cell by cell, all purely local dissipative processes: chemical reactions, thermo-chemical energy exchanges, equipartition and cooling. All these processes are described by very stiff equations. They imply necessarily very short time-steps, which would slow down dramatically the whole simulation and increase the CPU-time up to prohibiting values. Consequently to avoid this time-step catastrophe, we solve these stiff equations by using n consecutive sub-steps. At each sub-step and for each cell, we invert a 6×6 matrix for chemical reactions of the 6 involved species and a 3×3 matrix for the entropies. Our algorithm is fully vectorized and very effective, allowing high accuracy and stability. The number of sub-steps depends on the physical state of the cell. A similar method was used by Anninos and Norman (1994). Such a method is not justified as soon as the time scale of dissipative processes is much shorter than the dynamical time scale given by the Lagrangian step. This happens in very dense regions where cooling can be then overestimated. We discuss how to avoid such a mistake in Chièze, Alimi & Teyssier (1998). In the Eulerian low resolution case presented here, this happens only in one or two cells at the pancake center. However, using the prescription presented in Chièze, Alimi & Teyssier (1998) (which consists essentially to turn off line cooling in the central cell only), we find that cooling at small scales has little influence on the large scale flow.

2.9. Numerical Tests

2.9.1. Advection Test

This test was proposed by Stone & Norman (1992) to qualify the advection scheme only. We consider a box of length unity filled with a gas of homogeneous density. With a resolution of $N = 512$ cells and periodic boundary conditions, we model the advection at constant velocity of a single square pulse of density 10, initially sampled by 50 cells. Our results obtained with the three different projection schemes are very close to those obtained by Stone & Norman (1992) at the time when the pulse has crossed half of the computational space. The Donor cell interpolation is dramatically diffusive, while the two other schemes reproduce the sharp features relatively well.

2.9.2. Shock Tube Test

This test, also called the classical Riemann problem, is may be the most widely used to qualify hydrodynamics codes (Sod 1978). The initial conditions we use here are similar to those used by Stone & Norman (1992). We consider a box of size $L = 1$, $N = 128$ cells and $u = 0$. We separate the box in two regions (left and right) with the following conditions $\rho_L = 1$, $p_L = 1$ and $\rho_R = 0.125$, $p_R = 0.1$. We assume $\gamma = 1.4$ and reflective boundary conditions. We use for this test the quadratic term of the artificial viscosity only, with $C_1 = 0$ and $C_2 = 3$. In figure (1), we plot the different profiles obtained at time $t = 0.245$ for our standard simulation parameters, namely a Courant safety factor $C_0 = 0.5$, the Van Leer advection scheme and our second order time integrator. The results of our code is comparable to other methods, and very close to the analytical solution. Note however that the specific energy in the post-shock region is slightly better reproduced here than for example in Stone & Norman (1992). We think that this better agreement is mainly due to our second order time integrator.

To analyze the effect of our second order time integrator, we run the same simulation, but with a Courant safety factor $C_0 = 1$, which is the ultimate possibility. We plot in figure (2) the specific energy profiles obtained at time $t = 0.245$ for the three different advection schemes (Donor Cell, Van Leer and Piecewise Parabolic) using the second order time integrator, together with the profile obtained with the Van Leer advection scheme, but using the first order, explicit method. Note that in this latter case the solution is strongly unstable, while for the three former cases, the solution is identical to the $C_0 = 0.5$ case. This illustrates the interest of our second order time integrator. We also learn from this figure that the Donor Cell advection scheme is dramatically diffusive, and is practically of no use. The improvement of the solution from the Van Leer to the Piecewise Parabolic scheme is real, but not very dramatic, although for the latter the computational cost is

much higher. This justify the use of the Van Leer method as a standard choice.

2.9.3. Blast Waves Test

This test was used by Woodward & Colella (1985) to compare different hydrodynamics codes. It is may be the most adapted test for cosmological applications, because strong shocks are generated with Mach numbers $\simeq 10^5$ and are interacting violently. The initial conditions we use are the following (see Stone & Norman 1992) $L = 1$, $N = 1200$ cells, $\rho = 1$ and $u = 0$. In the left tenth of the box, we put $p = 1000$, in the right tenth $p = 100$ and in the middle $p = 0.01$. We assume $\gamma = 1.4$ and reflective boundary conditions. To have a more precise description of the different features involved in this simulation, see Woodward & Colella (1985). For this test, the linear term of the artificial viscosity is necessary to damp small oscillations occurring otherwise after strong shock fronts (we assume $C_1 = 1$ and $C_3 = 3$). We consider a Courant safety factor $C_0 = 0.5$ and our second order time integration scheme. Had we decided to use here the first order time integrator (explicit method), the Courant safety factor would have been $C_0 \simeq 0.1$ in order to recover similar results. We show in figure (3) the density profiles obtained at time $t = 0.038$ in order to compare with Stone & Norman (1992) and Woodward & Colella (1985). At that time, the two shock waves have already interacted at $x \simeq 0.7$ and are moving back to their original positions. The Piecewise Parabolic scheme presents the best agreement with Woodward & Colella (1985) reference simulation, although Van Leer results appears to be very similar too. As already mentioned, Donor cell scheme is unable to handle correctly sharp discontinuities, but more dramatic is the bad positioning of the shock fronts. During this run, total energy conservation was for Donor cell, Van Leer and PPI schemes respectively 7.6%, 2.1% and 1.1%.

3. PANCAKES COLLAPSE

3.1. Initial Conditions

We take for all runs the same initial conditions, beginning at epoch $z_i = 200$ where matter and radiation are well decoupled. The total density contrast has the following distribution

$$\delta(x) = \frac{a_i}{a_c} \cos\left(2\pi\frac{x}{L}\right) \quad (26)$$

and the baryons density distribution is taken equal to $\rho_B(x) = \bar{\rho}_B (1 + \delta(x))$. Dark matter particles are then moved according to Zel’dovich approximation, with the displacement field corresponding to the above density contrast. Initial velocity field for baryons is given by the linear growing mode

$$u_x(x) = -\frac{\Omega^{0.6}}{a} \partial_x \phi \quad (27)$$

The temperature for ions, electrons and neutral particles are chosen uniform and equal to $T_{e,i,n}(x) = T_0 (1 + z_i)$, where $T_0 = 2.7$ K is the cosmic radiation background temperature today. We suppose that the helium mass fraction is $Y = 0.24$. The initial ionization fraction are taken from Peebles (1993). In all our runs, we take $\Omega = 1$ and $H_0 = 50 \text{ km s}^{-1} \text{ Mpc}^{-1}$. Therefore, the single cosmological parameter of interest here is Ω_B . We have adopted periodic boundary conditions to ensure total mass conservation. We used Van Leer projection scheme since it is a good compromise between accuracy and CPU time and a Courant safety factor $C_0 = 0.5$. We consider in the following a reference pancake defined by a comoving length $L = 16 \text{ Mpc } h^{-1}$, a collapse epoch $a_c = 0.2$ and a baryon density parameter $\Omega_B = 0.1$.

3.2. Adiabatic Collapse

In this standard case, the gas is assumed to be fully ionized, and described by a single kinetic temperature. Sunayev & Zel’dovich (1972) and Bond *et al.* (1984) have derived analytically density and temperature profiles in that case. They have shown that a shock wave appears *off center* at a very small radius (typically a few 10^{-6} Mpc) which corresponds to the sonic radius. The flow is almost hydrostatic in this inner, unshocked region of high density contrast. The accretion shock front propagates outward, leaving an almost uniform pressure all over the accreted gas. Here, contrary to Bond *et al.* (1984) and Shapiro & Struck-Marcell (1985), we don’t resolve this very central region, because we are using a regular mesh (this mesh has been chosen in such a way to describe better the large scale, outer region of the pancake). We are aware of the fact that the better is the resolution, the higher is the density contrast in the central cell, until the resolution corresponding to the sonic radius is reached. For adiabatic runs, this has no incidence on the general aspect of the flow, since the pressure is almost uniform, in contrast with non adiabatic runs. We present in figure (4) velocity, temperature, pressure and baryons density profiles at $z = 0$ for various mesh resolution. It can be seen, besides an increasing sharpness of the shock front and an increasing density contrast in the central cell, that the resolution

has little quantitative influence on the results. The velocity field is typical of an accreting quasi-hydrostatic flow. The usual self-similar scaling laws ($T_{ad} \propto x^{2/3}$, $n_{ad} \propto x^{-2/3}$ and $P_{ad} \simeq const$) are well reproduced.

3.3. Non Adiabatic Collapse

We turn now to the analysis of non adiabatic pancake collapse, focusing on the temperature structure in the flow resulting from the microscopic collisional processes among the various species. We examine both the effects of energy exchange processes and of electronic conduction.

3.3.1. No Electronic Conduction

We follow precisely chemical reactions with the corresponding thermochemistry, collisional cooling processes and equipartition processes, as discussed in Section 2. We first suppose that electronic conduction is ineffective. Figure (5) shows that the electronic temperature decouples from the ion temperature at $600 \text{ kpc } h^{-1}$ from the mid-plane. The maximum departure from equilibrium is found near the shock front at $1.1 \text{ Mpc } h^{-1}$. In this region, ion temperature is about 10^7 K when electron temperature barely reaches 10^6 K . Furthermore, the ion and electron temperature profiles are different, with opposite gradients: the electron temperature steadily drops towards the front, while the ion temperature rises.

Non equilibrium chemistry is required especially in the post-shocked regions in which ionization gradually reaches its *near-equilibrium* value. Recall that electrons are essentially heated behind the shock front by Coulomb collisions with hot ions. Since equipartition processes are conservative, the total energy density (i.e. the total pressure) is unchanged relative to the single temperature case. By themselves, equipartition processes do not affect the dynamics of the flow, which is only modified – relative to the adiabatic case – by cooling. Since the equipartition rates per particle are proportional to density, the temperature of ions and electrons are well coupled in the dense parts of the pancake, but significantly decouples in the low density outer regions. The equilibrium point (where T_e and T_i differ from less than 2%) will be roughly estimated by analytical calculations presented below.

3.3.2. Electronic Conduction

In that case, we suppose that electronic conduction is fully effective, with flux-limited diffusion (Cowie & Mc Kee 1977). We find that conduction is saturated only in the central region, where temperature gradients are very stiff, and in the most outer regions, where the density is very low. Computing thermal fluxes is a complicated task, since it depends on the ionization state of the gas, which in turn depends on the propagation speed of the ionizing thermal wave. We need therefore a good sampling of the ionization front to accurately track the thermal front. This explains why we decided to choose a linear mesh, in order to achieve a fair sampling of temperature and abundance profiles in the thermal wave.

We plot in figure (6) the pancake state at $z = 0$. Note that the ionization state of the gas is very well sampled and that abundances gradually evolve towards their equilibrium values. The shock front position at $1 \text{ Mpc } h^{-1}$ is very close to its position in the “no conduction” run. The main effect of conduction is the thermal precursor, which pre-heats and pre-ionizes the gas up to $1.5 \text{ Mpc } h^{-1}$ from the mid-plane. Because equipartition processes are slow in this region, ion temperature reaches only 10^5 K , while electron temperature is 10^6 K . Nevertheless, this results in a slight dynamical effect on the flow: ion pressure gradients cause a small deviation from the pressureless velocity profile in the unshocked region, clearly visible on this figure. Shock-heated regions occupy a total volume of $2 \text{ Mpc } h^{-1}$, while unshocked but pre-heated ($T_i \simeq 10^5 \text{ K}$) and pre-ionized ($T_e \simeq 10^6 \text{ K}$) regions occupy a total volume of $1 \text{ Mpc } h^{-1}$. As we will see in the next part, the efficiency of electronic conduction depends strongly on the pancake size.

3.4. Varying the Pancake Parameters

In this section, we study the influence of the different parameters on the pancake structure. We develop approximate formulae which guide us for our conclusions. We assume that, in any case, the dynamical state of the pancake is given by the adiabatic collapse. Following Bond *et al.* (1984) and Shapiro & Struck-Marcell (1985), it is then possible to derive interesting formulae for the pancake evolution.

We assume first that each fluid element q is shock-heated at an epoch given by

$$\frac{a_s}{a_c} = \frac{\pi q}{\sin \pi q} \quad (28)$$

This corresponds to the epoch when the corresponding collisionless particle crosses the center of the pancake. We suppose also that the gas is fully ionized and that the flow

remains strictly adiabatic. Before the shock front, the flow follows the pressureless solution of pancake collapse (Zel'dovich 1970). Using Rankine-Hugoniot relations and *assuming that the post-shock peculiar velocity vanishes*, we get the post-shock temperature and the post-shock overdensity

$$kT = \frac{1}{12}\mu m_p a^{-1}(H_0 L)^2 q^2 \quad (29)$$

$$1 + \delta = 4 / \left(1 - \pi q \frac{\cos \pi q}{\sin \pi q} \right) \quad (30)$$

As we assumed that the peculiar velocity is zero in the post-shock region, the temperature evolves afterwards as a^{-2} and the density as a^{-3} . Mass conservation implies also that the Eulerian position of a given fluid element in the shocked region is given by

$$x = \int_0^q \left(1 - \pi q \frac{\cos \pi q}{\sin \pi q} \right) \frac{dq}{4} \quad (31)$$

This allows us to describe the dynamical evolution (single temperature case) of the pancake. Let us now estimate the thermodynamical evolution using our three temperatures formalism. The equipartition time-scale for electron-ion energy exchange is given by

$$t_{ei} = 503 \frac{T_{ei}^{3/2}}{n_e \ln \Lambda} \text{ sec.} \quad (32)$$

Assuming that the effective temperature T_{ei} is equal to the post-shock adiabatic temperature, the equipartition time-scale remains then constant during the post-shock evolution (we neglect the slow variation of the Coulomb logarithm, taking $\ln \Lambda \simeq 40$). It is now possible to solve analytically the equipartition equation

$$\frac{d}{dt} (T_e - T_i) + 2 \frac{\dot{a}}{a} (T_e - T_i) = - \frac{4}{t_{ei}} (T_e - T_i) \quad (33)$$

The single temperature, given by equation (29), is related to T_e and T_i by

$$T = \frac{n_e T_e + n_i T_i}{n_e + n_i} \quad (34)$$

We finally obtain semi-analytical temperatures profiles, plotted in figure (7), for the reference pancake at $z = 0$. Note that numerical results agree qualitatively well with

our analytical theory. Because we assumed that the post-shock velocity vanishes, we overestimate the shock front position and the post-shock temperature. In the numerical calculation, Lagrangian fluid elements pile up deeper than we assume in our analytical calculation. This explain the visible differences between numerical and analytical results.

The pancake structure is fully described by three characteristic points, as we already presented in the upper sections: the *compression point* where ions and neutral particles are shocked, the *thermal point* which marks the end of the thermal wave and the *equilibrium point* where equilibrium between electrons and ions is recovered. In the small q limit, Bond et al. (1984) derived the Lagrangian coordinate of the compression point

$$q_s \propto \left(1 - \frac{a_c}{a}\right)^{1/2} \quad (35)$$

We can write, assuming that $a - a_c \ll a_c$

$$q_s \propto \left(\frac{a - a_c}{a_c}\right)^{1/2} \quad (36)$$

We derive here (for $q \ll 1$ and $a - a_c \ll a_c$) the Lagrangian coordinate of the equilibrium point (where electrons and ions temperatures differ from only 2%)

$$q_{eq} \propto \left(\frac{a - a_c}{a_c}\right)^{1/5} L^{-3/5} \Omega_B^{1/5} \quad (37)$$

It appears that this coordinate depends strongly on the pancake size. This is due to the strong dependence on temperature ($T^{3/2}$) of the equipartition time-scale. When the baryon density parameter is decreased from 0.1 to 0.01, the equilibrium point reaches much deeper regions. The final mass at thermodynamical equilibrium is about 85% of the total shock-heated mass for the $\Omega_B = 0.1$ case, and decreases to about 50% for the $\Omega_B = 0.01$ case. The time-dependence of the equilibrium point is much slower than for the shock front. This means that non-equilibrium features appear mainly at late epoch and in the most outer regions where density has decreased (and temperature has increased) sufficiently.

Formula (37) is valid only for the small q regime. To test the validity of our description at later epoch (the large q regime), we run numerical calculations with different pancake sizes. All these runs were computed assuming that electronic conduction is effective, and that $\Omega_B = 0.1$, $a_c = 0.2$. We plot in figure (8) the shock front Eulerian position x_s , the equilibrium point position x_{eq} and the thermal front position x_{th} obtained in these simulations. The shock front position is almost independent of the pancake size, as expected

by formula (36). The equilibrium point is found in deeper regions as L increases, as expected by formula (37). The thermal wave has approximately the symmetrical behavior than the equipartition wave.

For $L \simeq 10 \text{ Mpc } h^{-1}$, cooling starts to be important and the flow does not remain adiabatic. The main consequence is that the compression point propagates outwardly at a lower velocity than for the adiabatic case. This characteristic pancake length corresponds roughly to pancakes for which the *average* cooling time is equal to the Hubble time. Indeed, assuming that the mean temperature is given by equation (29) with $q = 1/4$, $\bar{\delta} \simeq 10$ and using the *equilibrium* cooling curve to calculate the cooling rate, we find $L_{cool} \simeq 8 \text{ Mpc } h^{-1}$.

4. CONCLUSIONS

In this paper, we use a three temperature formalism to describe the thermodynamical evolution of pancakes. We show that the assumption of thermodynamical equilibrium between ions and electrons is not valid in the outer regions of pancakes. The corresponding temperature profiles show differences up to one order of magnitude near the shock front and reach thermodynamical equilibrium near the centre, where the overdensity is $\delta \simeq 10$. Electrons and ions decoupling is stronger for large pancake sizes or for low Ω_B . This could have observational consequences for X-ray temperature profiles. The dynamical (total) pressure in the outer regions of clusters can differ from the observed electrons pressure up to one order of magnitude. This effect can be even stronger for non-relaxed clusters, where recent mergers strongly decoupled electrons and ions through shocks. This could lead to an underestimate of the cluster mass in this regions. In the central hydrostatic part of clusters, where thermodynamical equilibrium is efficiently recovered, such effect are not likely to appear. We address this question using a fully 3D X-ray clusters modeling in a companion paper (Chièze, Alimi & Teyssier 1998)

In the outermost regions, we show that electronic conduction, if effective, leads to a thermal wave escaping the shock-heated regions of the pancake. This thermal precursor could have interesting cosmological consequences, such as late reionization and heating of non collapsed regions. In our case, the precursor is strongly confined by the very high infall velocity towards the pancake centre. In a more complex geometry, one can imagine that the size of the precursor could be much more extended, leading to efficient heating of the intergalactic medium. This effect might be detected in the vicinity of very large X-rays clusters.

Non-equilibrium regions (from the thermal precursor to the equilibrium point) are

very extended and dominate *in volume* the structure of pancakes (this paper) and X-ray clusters (Chièze, Alimi & Teyssier 1998). Using high sensitivity experiments, like the X-ray satellite XMM (Fabian 1987), we will be able in the future to observe the low density part of clusters, where all these processes are likely to be very important.

The authors would like to thank an anonymous referee for the constructive remarks that allow us to increase the quality of our work.

REFERENCES

- Annios, W.Y., & Norman, M.L., 1994, ApJ, 429, 434.
- Bond, J.R., Centrella, J. Szalay, A.S., & Wilson, J.R., 1984, MNRAS, 210, 515.
- Cen, R.Y., 1992, ApJS, 78, 341.
- Cen, R.Y., & Ostriker J.P., 1992, ApJ, 393, 22.
- Chièze, J.-P., Alimi, J.-M. & Teyssier, R., 1998, ApJ, 495, 630.
- Chièze, J.-P., Pineau des Forêts, G. & Flower, D.R., 1998, MNRAS, 295, 672.
- Chièze, J.-P., Teyssier, R., & Alimi, J.-M., 1997, ApJ, 484, 40.
- Cowie, L.L., & McKee, C.F., 1977, ApJ, 211, 135.
- Draine, B.T., 1980, ApJ, 246, 1045.
- Draine, B.T., & Katz, N., 1986, ApJ, 306, 655.
- Fabian, ,A.C., 1987, “Starburst and Galaxy Evolution”, p. 581, XXII Moriond Astrophysics, Les Arcs, France, (Editions Frontieres).
- Hockney, R.W., & Eastwood, J.W., 1981, “Computer Simulations Using Particles” (New York McGraw-Hill).
- Markevitch, M, Mushotzky, R, Inoue, H, Yamashita, K, Furuzawa, A. & Tawara, Y., 1996, ApJ, 456, 437.
- Peebles, P.J.E. 1980, “The Large Scale Structure of the Universe” (Princeton: Princeton University Press).
- Peebles, P.J.E. 1993, “Principles of Physical Cosmology” (Princeton: Princeton University Press).

Shapiro, P.R., & Struck-Marcell, C., ApJS, 57, 205.

Sod, G., 1978, J. Comput. Phys., 27, 1.

Spitzer, L., 1962, “The Physics of Fully Ionized Gases” (Interscience, New York).

Stone, J.M., & Norman, M.L., 1992, ApJS, 80, 753.

Tucker, W.H., 1975, “Radiation Processes in Astrophysics” (MIT Press, Cambridge, Massachusetts).

Woodward, P.R. & Colella, P., 1985, J. Comput. Phys., 54, 115.

Zel’dovich, Ya. B., & Raizer, Yu. P., 1966, “Physics of Shock Waves and High-Temperature Hydrodynamic Phenomena” (Academic Press, New York).

Zel’dovich, Ya. B., 1970, A&A, 5, 84.

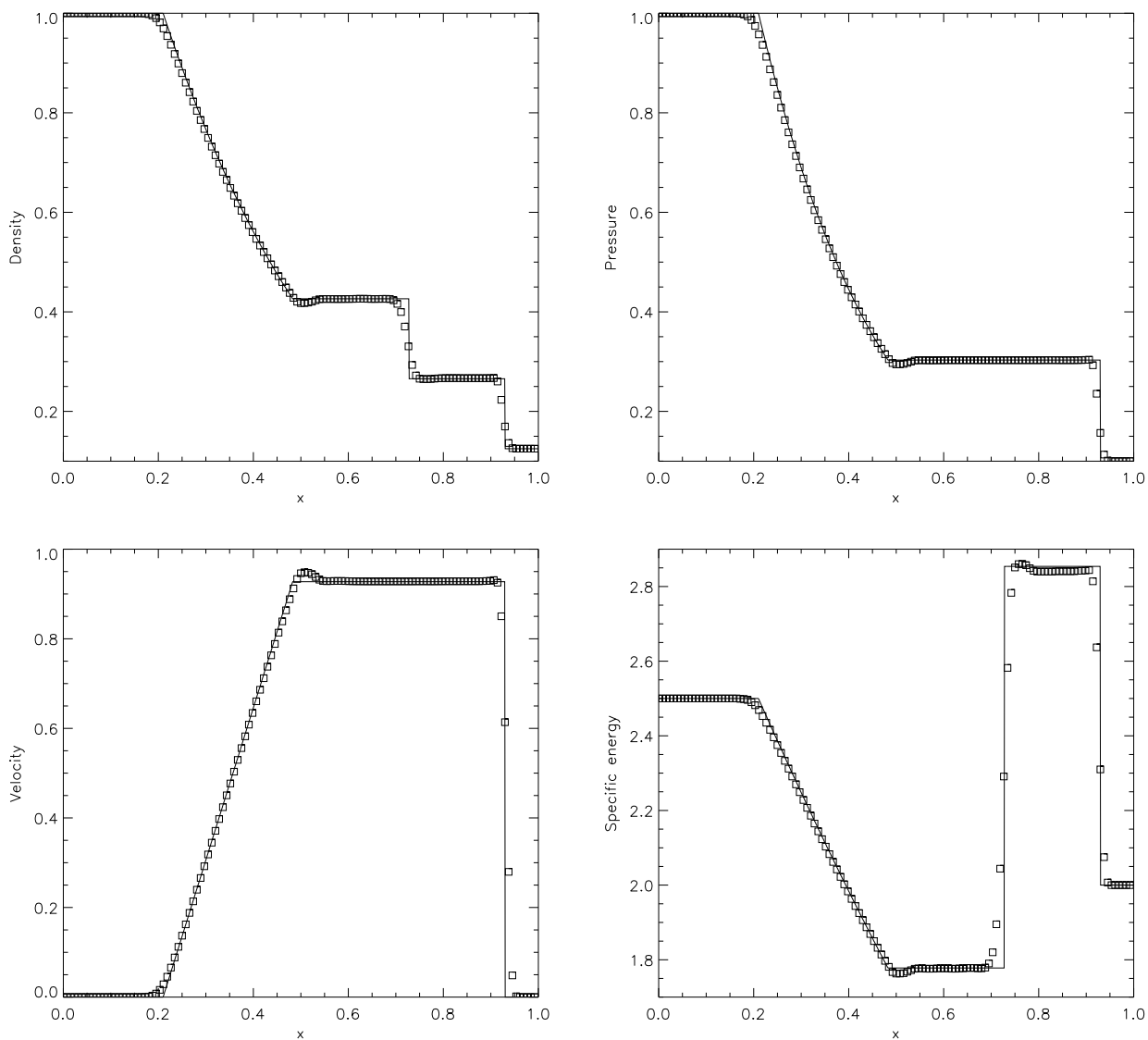


Fig. 1.— Density, pressure, velocity and specific energy profiles obtained for the shock tube test at time $t = 0.245$. We use for that run our standard parameters: Van Leer advection scheme, second order time integrator, Courant safety factor $C_0 = 0.5$. The analytic profiles are shown as solid lines.

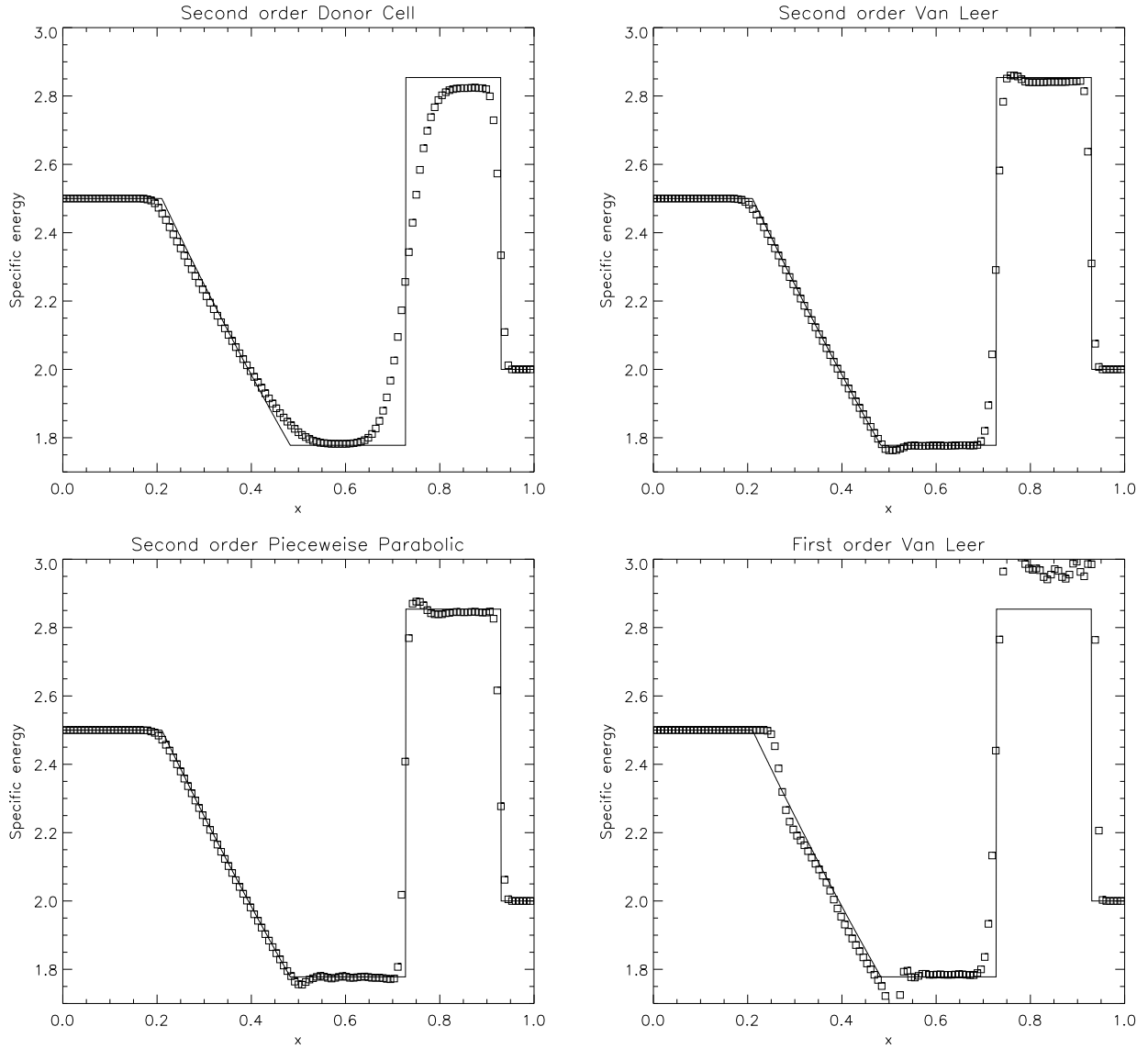


Fig. 2.— Specific energy profiles obtained with the shock tube test for different advection schemes, second order time integration and the “ultimate” Courant safety factor $C_0 = 1$. We also plot the solution obtained with the explicit method (first order) for the same Courant safety factor. The analytic profile is shown as the solid line in each graph.

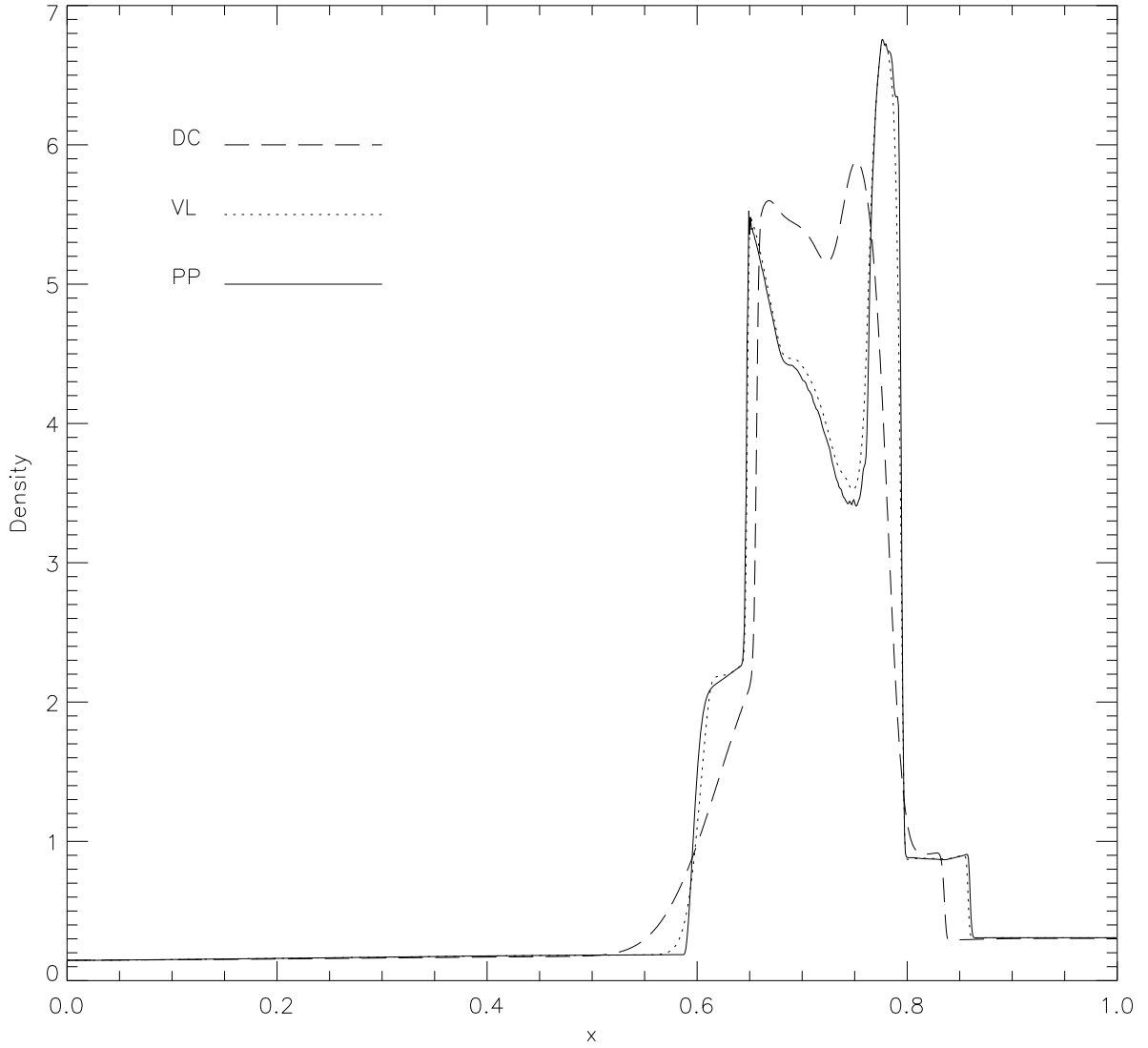


Fig. 3.— Density obtained with the blast waves test for different projection schemes Donor cell (dotted line); Van Leer (dashed line); Piecewise Parabolic (solid line). We use second order time integration and a Courant safety factor $C_0 = 0.5$.

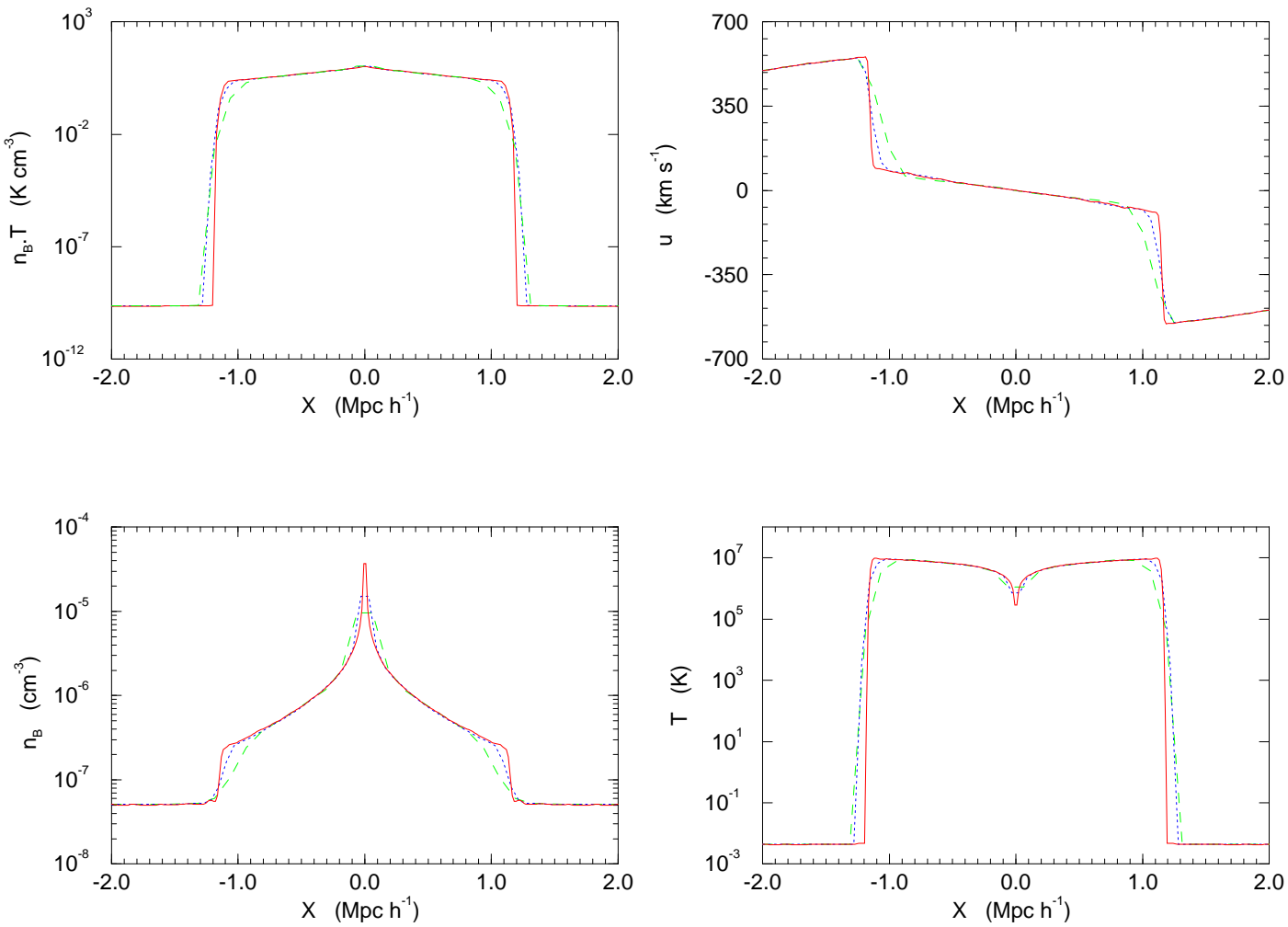


Fig. 4.— Density, velocity, temperature and pressure profiles at $z = 0$ for the adiabatic collapse of the reference pancake ($L = 16 \text{ Mpc } h^{-1}$, $a_c = 0.2$ and $\Omega_B = 0.1$). In each graph we plot three runs with increasing resolution ($N=128$: dashed line, 256: dotted line and 1024: solid line).

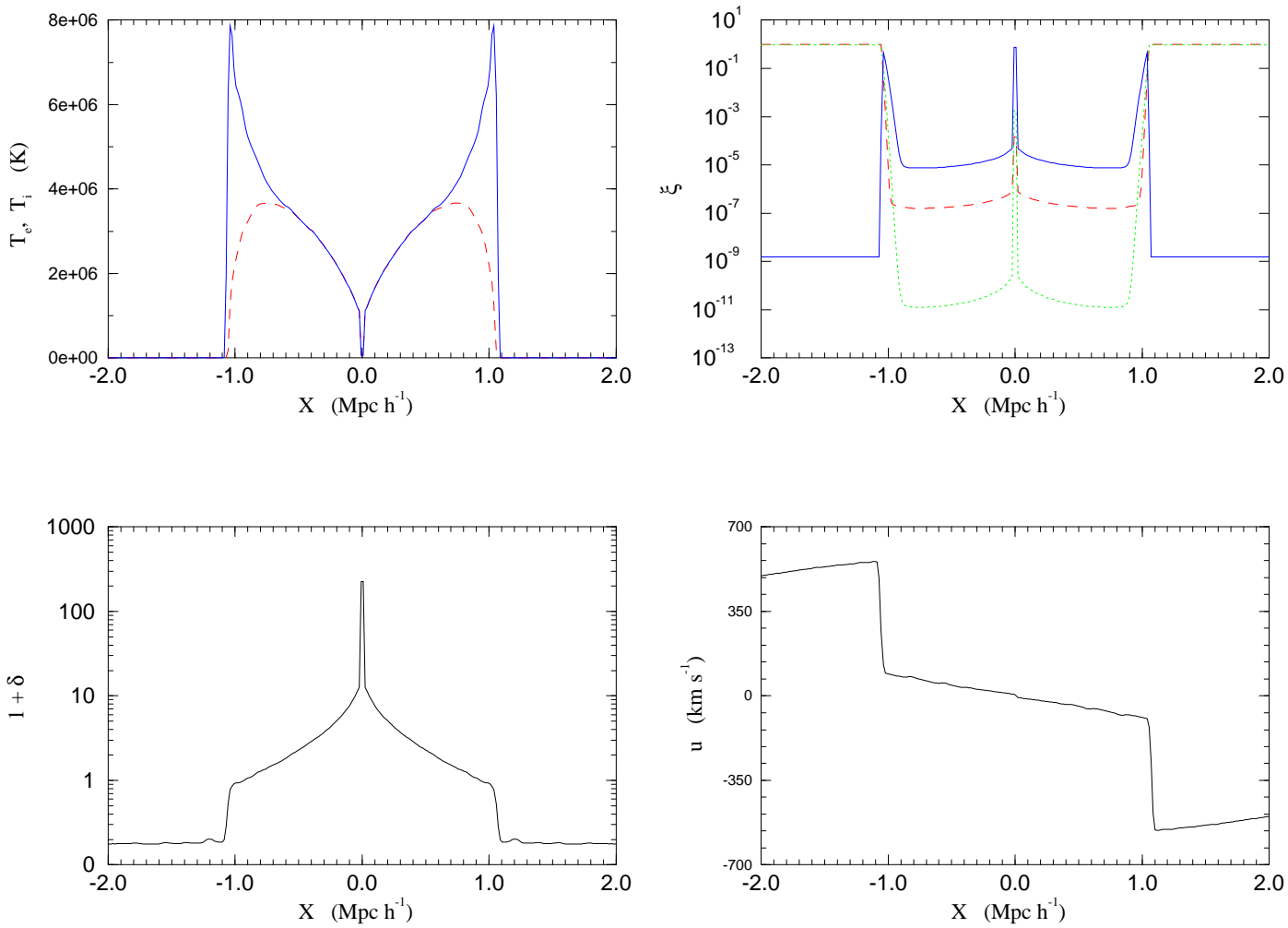
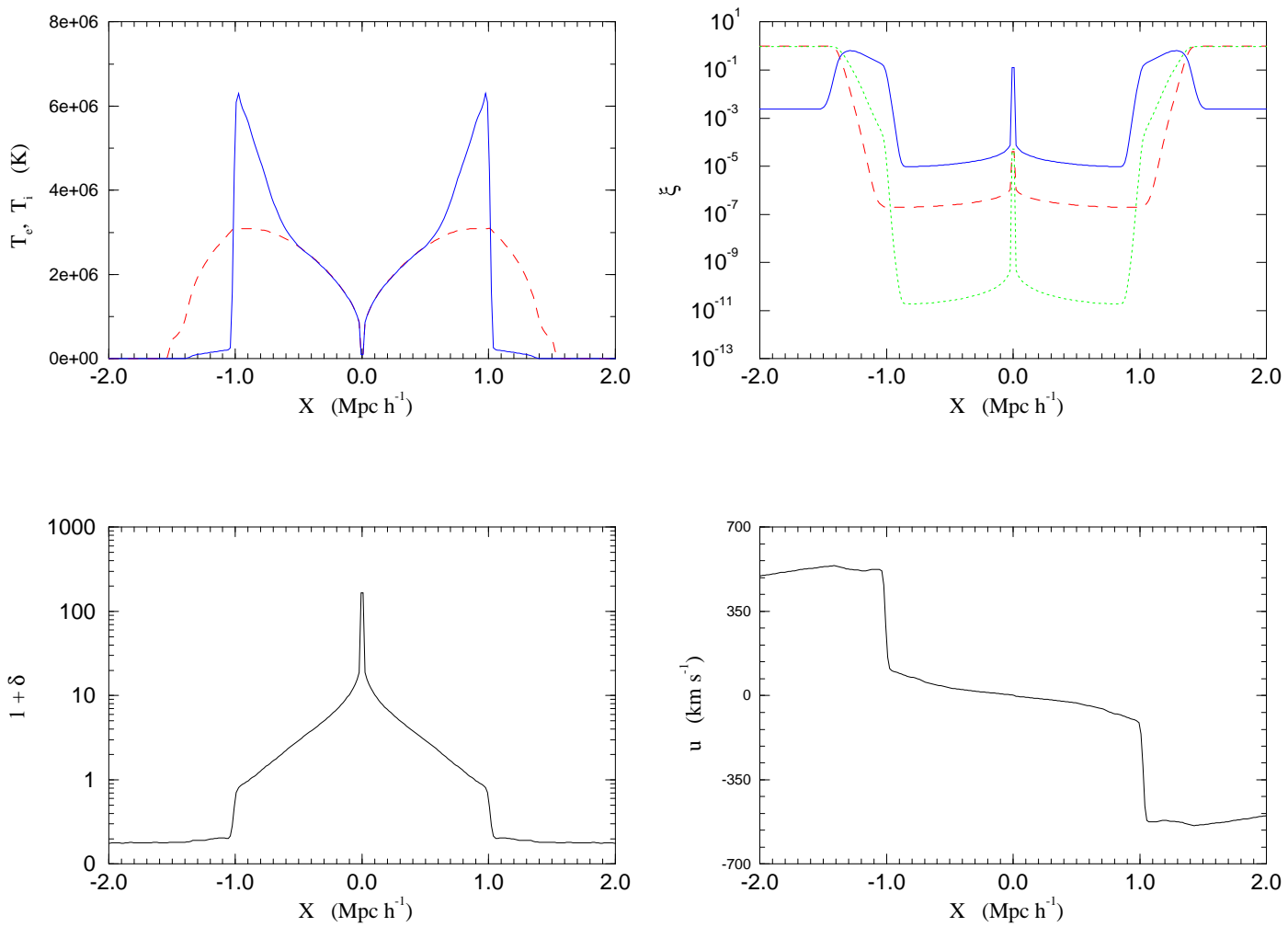


Fig. 5.— Gas overdensity and velocity, ions (solid line) and electrons (dashed line) temperatures, ionization fraction for HI (dashed line), HeI (dotted line), and HeII (solid line) at $z = 0$ for the reference run without electronic conduction.

Fig. 6. — Same as figure (5) for the reference run with electronic conduction.



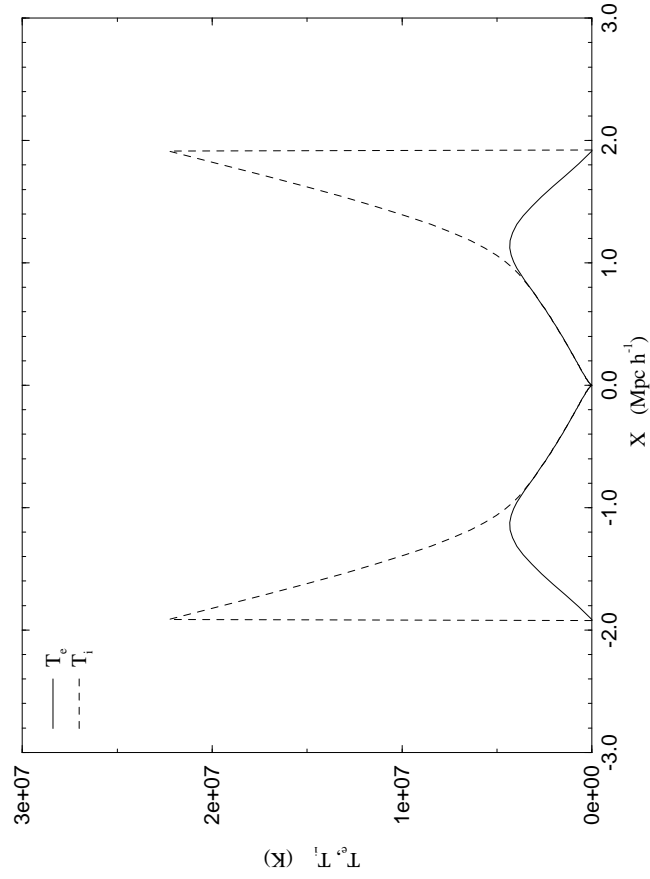


Fig. 7.— Analytical ions (dashed line) and electrons (solid line) temperatures profiles for the reference pancake at $z = 0$. Compare this figure to the numerical results obtained in figure (5).

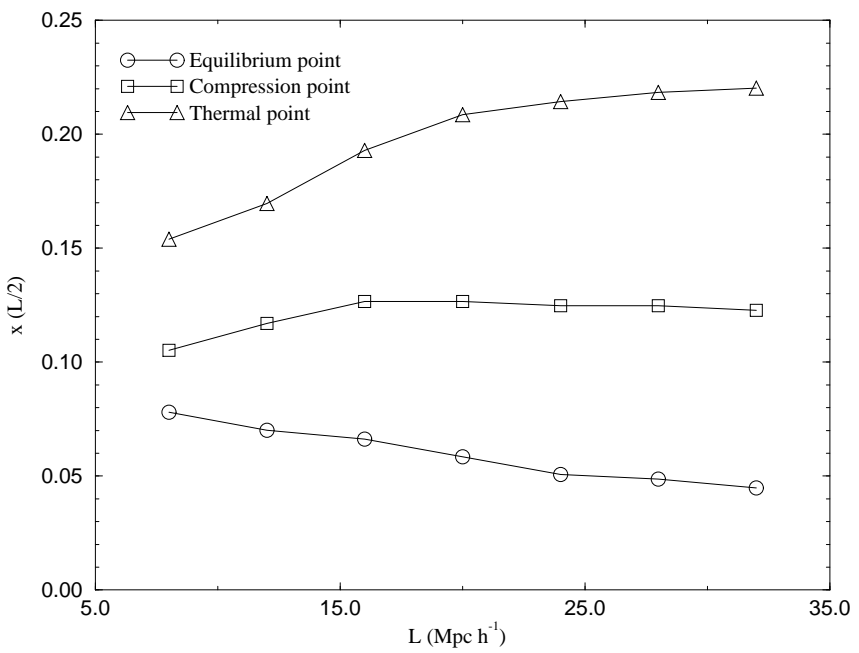


Fig. 8.— Eulerian comoving coordinates of the three characteristic points (see text) which describe non-equilibrium features in the flow for various pancake sizes.